Supplementary Material

Design principles for fluoroethylene carbonate additive-electrode compatibility in nanoporous sugarcane bagasse based hard carbon sodium ion anodes

Jiahan Fu,[a] Sheng Li,[a] Chaofan Luo,[a] Honglin Hu,[a] Tianshun Xiong,[a] Xin Li,[a] Junyou Yang,[a] Guangwei Huang,[b] Jianfang Li,[b] Yubo Luo,*[a] Canhuang Zhang*[b]

[a]State Key Laboratory of Materials Processing and Die & Mould Technology, School of Materials Science and Engineering, Huazhong University of Science and Technology, Wuhan 430074, P. R. China. luoyubo@hust.edu.cn (Y. Luo).

[b]Guangxi Huangguan Energy Storage Technology Co., Ltd, Qinzhou 535000, P. R. China. 418180760@qq.com (C. Zhang).

1.Experimental section

1.1Materials

Raw sugarcane bagasse was sourced from a local fresh produce company in Guangxi Province, China. The material was thoroughly washed several times with deionized water and subsequently dried in a hot-air oven at 85 °C for 72 hours. The dried sugarcane bagasse was then ground using a mechanical grinder and sieved to pass through a 100-mesh screen. BHC, LHC, and KHC refer to commercial hard carbon samples obtained from different suppliers. Specifically, BHC was sourced from BTR (model BHSC-300), LHC from Shanshan Tech (model LHC-5F), and KHC from Kuraray (model Type 3). All chemicals used in this study were of analytical grade and used as received without further purification. Deionized water was employed throughout all experimental procedures.

1.2 Preparation of sugarcane bagasse-based Hard Carbon

A total of 2 g of the pretreated sugarcane bagasse powder was placed in a tubular furnace and heated under a nitrogen (N_2) atmosphere. The temperature was first increased to 300 °C at a ramp rate of 2 °C min^{-1} and held for 2 hours for pre-carbonization. Subsequently, the samples were further heated to target temperatures of 800 °C, 1000 °C, and 1200 °C at the same heating rate (2 °C min^{-1}) and maintained for 2 hours under flowing Ar. After carbonization, the furnace was allowed to cool naturally to room temperature. The resulting carbon materials were denoted as SuHC-800, SuHC-1000, and SuHC-1200, corresponding to their respective carbonization temperatures.

1.3 Sample characterizations

The morphology of the samples was examined using a field-emission scanning electron microscope (FE-SEM, Nova NanoSEM 450, FEI, Netherlands). The microstructure was further investigated by a field-emission transmission electron microscope (TEM, JEM-ARM200F, JEOL, Japan) and a high-resolution transmission electron microscope (HRTEM). Phase composition and structural parameters of the hard carbon samples, were analyzed via powder X-ray diffraction (XRD) using an Empyrean diffractometer

(PANalytical B.V., Netherlands) equipped with a Cu Kα radiation source (λ = 0.15432 nm, D8 Advance, Bruker, Germany). Raman spectroscopy was performed using a LabRAM HR800 Raman spectrometer (Horiba Jobin Yvon, France) to analyze the structure of the carbon materials and electrolytes. Nitrogen adsorption–desorption isotherms were measured on a 3Flex surface area and porosity analyzer (Micromeritics, USA; model: Isorb-HP2) to determine the specific surface area and pore size distribution of the samples. X-ray photoelectron spectroscopy (XPS) was performed using an AXIS SUPRA+ spectrometer (Shimadzu–Kratos, Japan) to analyze the surface chemical composition of the electrode samples. The electrodes were harvested from disassembled cells and washed three times with pure dimethyl carbonate (DMC) to remove residual sodium salts. All samples were subsequently dried under argon atmosphere in a glove box and vacuum-sealed to avoid exposure to air and moisture.

1.4 Electrochemical measurements

The electrode material, Super P, and polyvinylidene fluoride (PVDF) were dispersed with a mass ratio of 8:1:1 in N-methyl-pyrrolidone solvent (NMP) and stired to form a uniform slurry. The uniform slurry was then applied onto aluminum foil with a thickness of 12 um, and first placed in an oven for 1 hours, and then transfer it to a vacuum oven at 80 ℃ to dry for 12 h, then cutted into pole pieces with a diameter of 14mm finally. The average areal mass loading of the electrodes were approximately 2 mg cm^{-2}. CR2032 button type half-cell was assembled in a glove box with humidity and oxygen concentration below 0.01ppm. The assembly sequence is as follows: shrapnel and gasket were placed on the negative electrode shell, then added sodium metal plate as the counter electrode, dropped electrolyte (1M $NaPF_6$ in ethylene carbonate (EC): dimethyl carbonate (DMC)=1:1, v/v) or 1M $NaPF_6$ in ethylene glycol dimethyl ether (DME) or 1M $NaPF_6$ in EC：DMC with 2wt% fluoroethylene carbonate（FEC）or 1M $NaPF_6$ in DME with 2wt% FEC), and placed glass fiber membrane as diaphragm, then placed the prepared working electrode, and fastened the positive electrode shell finally, Pressed into a button type half-cell on a dedicated tablet press.

All samples were subjected to electrochemical performance characterization at room temperature of 25 ° C. The Neware BTS-CT-4000 battery testing system was used to testing the charging/discharging curves at various rates (0.03A g^{-1}-1.5A g^{-1}) within the voltage range of 0.01V-2.5V (ester-based electrolyte) and 0.01V-2.5V (ether -based electrolyte). The CV testing (0.01-2.5V) with a scanning rate of 0.1mV-2mV and EIS testing (frequency range of 0.01Hz-100kHz, amplitude of 5mV) were conducted with an electrochemical workstation (IGS4000, China).

1.5 Formula section

CV measurement was conducted at different scanning rates, and the peak current (i) and scanning speed (ν) comply with the following relationship:

$$i = a\nu^b \quad \textbf{(S1)}$$

$$\log i = \text{blog}\,\nu + \log a \quad \textbf{(S2)}$$

Where a and b are constants. The value of b determines the dominant behavior of electrode reactions, where b=0.5 represents diffusion-controlled reactions and b=l.0 represents capacitance-controlled reactions. If the b value is between 0.5 and 1.0, the electrochemical reaction is controlled by both capacitance and diffusion processes simultaneously.

the contributions of diffusion control and capacitance control storage mechanisms can be quantified by the following formula:

$$i = k_1\nu + k_2\nu^{1/2} \quad \textbf{(S3)}$$

Where k_1 and k_2 are constants.

1.6 Theoretical calculations section

In the molecular dynamic's simulations, The Forcite Module of Materials Studio software was used for all the calculations and the force fields of the atoms were COMPASSIII. A bulk system was created by packing structurally optimized molecules in a periodic box of size 41 x 41 x41 $Å^3$.[1] For system1 the simulation box contains 40 $NaPF_6$, 384 DME. For system2 it contains 32 $NaPF_6$, 132 DMC, and 240 EC. For system3 it contains 40 $NaPF_6$, 384 DME, and 8 FEC. For system4 it contains 32 $NaPF_6$, 132 DMC, 240 EC and 8 FEC. These data were set according to the experiment. The Summation method was employed by Ewald and atom based, respectively. Moreover, a Verlet algorithm was integrated with Newton's equations of motion at a time step of

1 fs for a total simulation time of 1000 ps, i.e. 1000000 steps. The frequency of the temperature oscillations was controlled via Nose-Hoover thermostat during the simulations in the canonical ensemble (NVT), Before the calculation of molecular dynamics, the NPT calculation of 500 ps is used for acquiring stable volume values at room temperature.[2]

The electronic structures of four representative solvent molecules—dimethyl carbonate (DMC), dimethyl ether (DME), ethylene carbonate (EC), and fluoroethylene carbonate (FEC)—were investigated via density functional theory (DFT) calculations. All molecular geometries were fully optimized using the B3LYP exchange–correlation functional in combination with the 6-311++G(d,p) basis set, as implemented in the Gaussian 16 software package. Frequency analyses were subsequently performed at the same level of theory to confirm the nature of the optimized structures as true minima (i.e., no imaginary frequencies).[3] The energies of the highest occupied molecular orbital (HOMO) and lowest unoccupied molecular orbital (LUMO) were extracted from the optimized structures to evaluate the relative reduction propensity of the solvents.

The adsorption behavior and energetics of NaF molecules on porous carbon were evaluated using density functional theory (DFT) as implemented in the Vienna Ab initio Simulation Package (VASP).[4] The exchange–correlation energy was treated within the generalized gradient approximation (GGA) using the Perdew–Burke–Ernzerhof (PBE) functional.[5] The interaction between ion cores and valence electrons was described using the projector augmented wave (PAW) method. A plane-wave cutoff energy of 500 eV was employed to ensure sufficient convergence accuracy. To account for van der Waals (vdW) interactions, Grimme's DFT-D3 dispersion correction scheme was applied. During structural relaxation and electronic calculations, the energy convergence criterion was set to 1×10^{-5} eV, and the maximum force acting on each atom was limited to 0.03 eV $Å^{-1}$. The Brillouin zone was sampled using a $3 \times 3 \times 1$ Monkhorst–Pack k-point mesh.[6] The adsorption energy (E_{ads}) of a NaF molecule on porous carbon was calculated using the following equation:

$$E_{ads} = E_{G+NaF} - E_G - E_{NaF} \quad \textbf{(S4)}$$

where E_{G+NaF} is the total energy of the porous carbon system with adsorbed NaF, E_G is the energy of the clean porous carbon substrate, and E_{NaF} is the energy of an isolated NaF molecule optimized under the same conditions. This calculation allows for a quantitative comparison of NaF adsorption preference between different carbon sites, including surface and confined pore environments.

2. Supplementary Figures

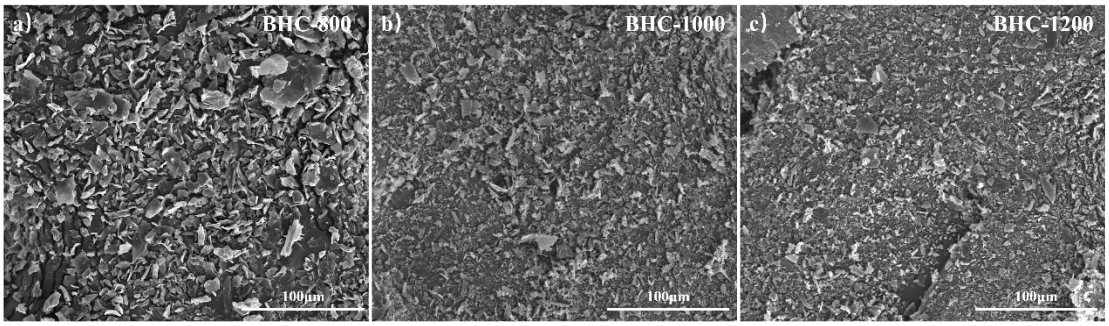

Fig. S1. SEM images of (a) SuHC-800. (b) SuHC-1000. (c) SuHC-1200.

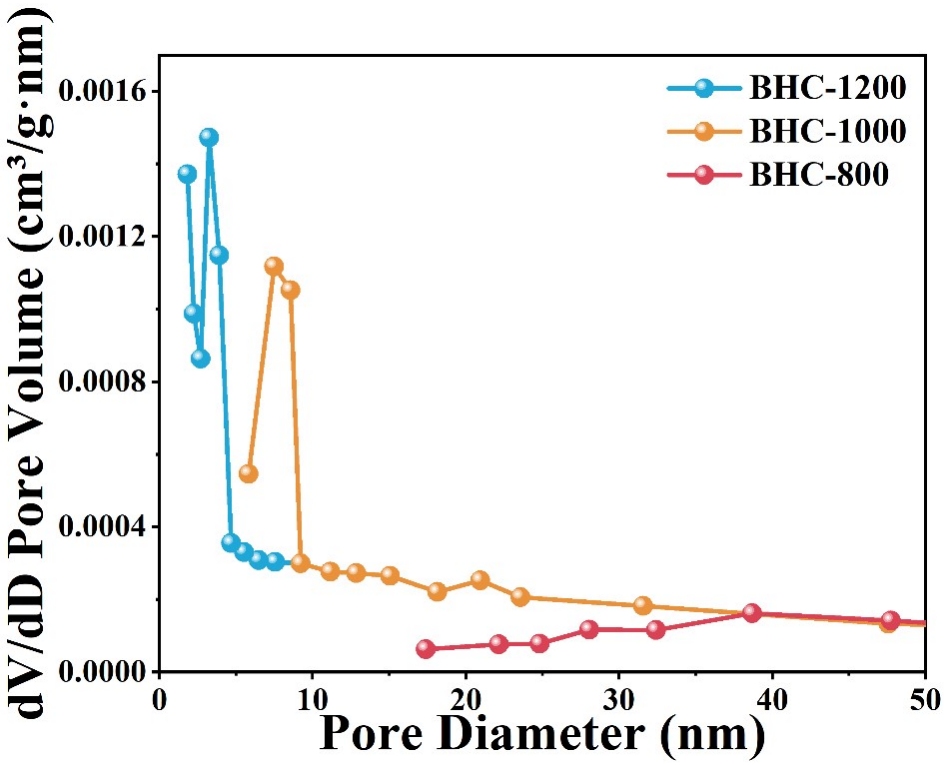

Fig. S2. The pore size distribution of all sample

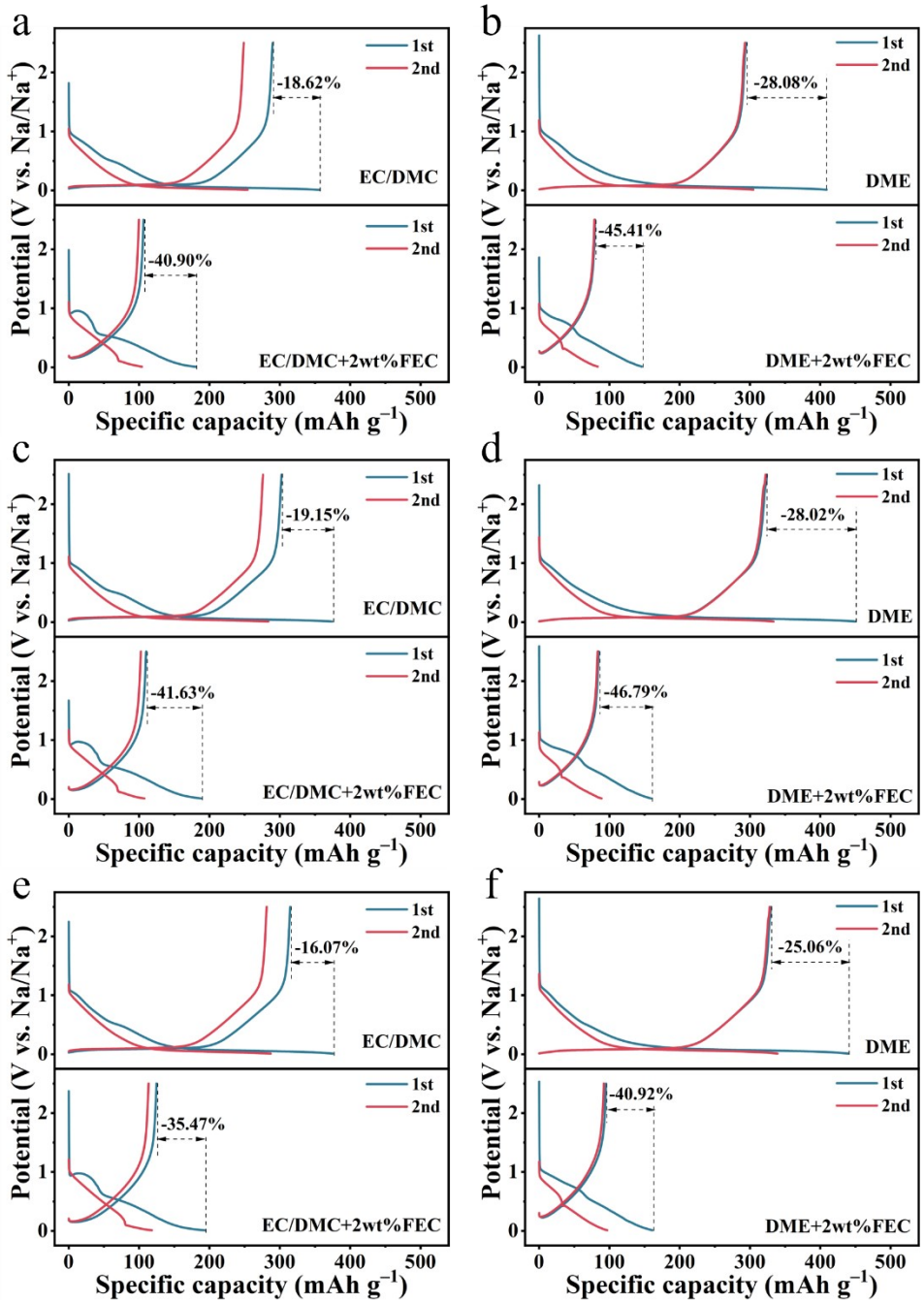

Fig. S3. Charge-discharge curves of the half cell during the first two cycles of BHC a) EC/DMC and EC/DMC+2wt%FEC and b) DME and DME+2wt%FEC; Charge-discharge curves of the half cell during the first two cycles of LHC c) EC/DMC and EC/DMC+2wt%FEC and d) DME and DME+2wt%FEC; Charge-discharge curves of the half cell during the first two cycles of KHC c) EC/DMC and EC/DMC+2wt%FEC and d) DME and DME+2wt%FEC.

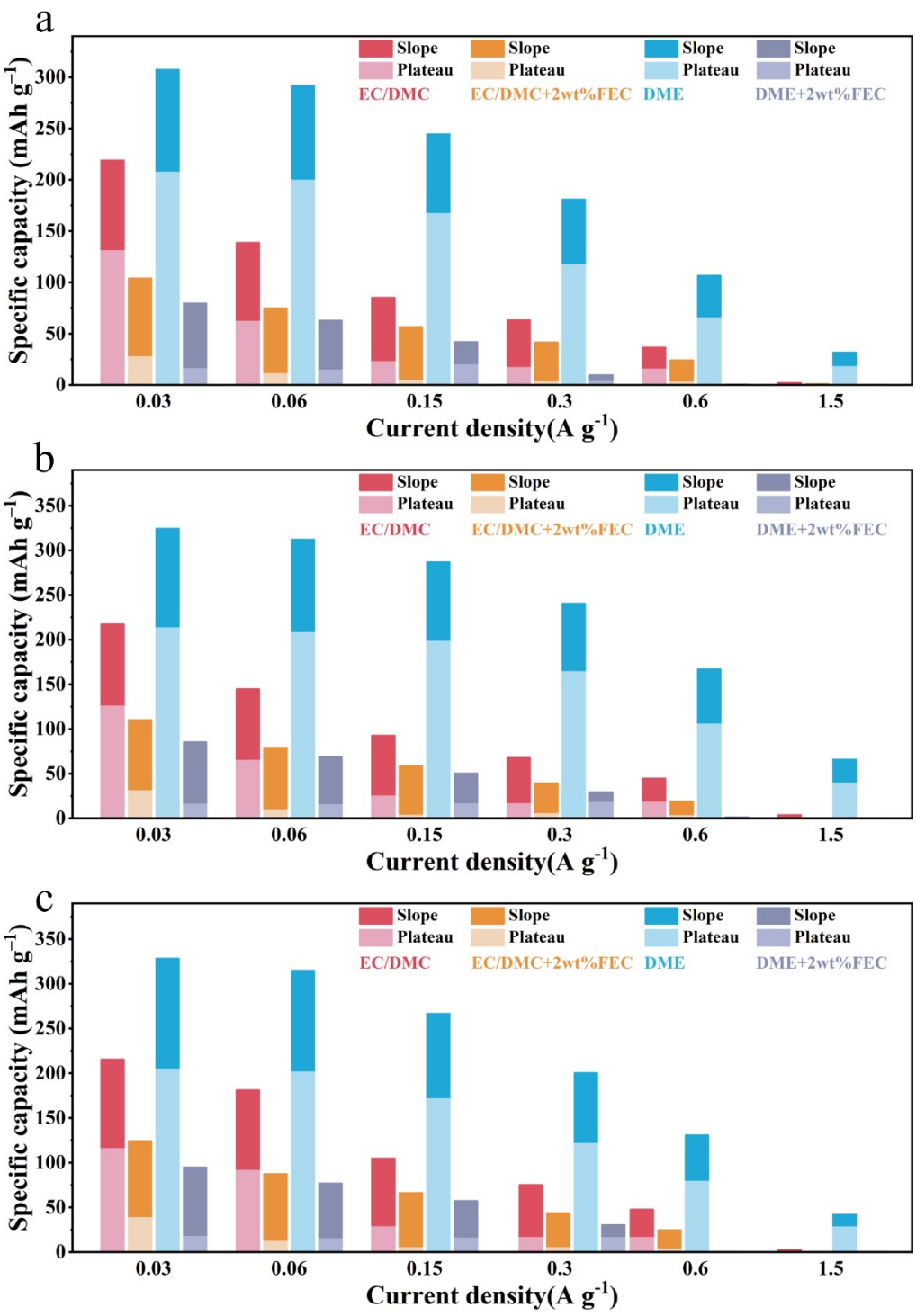

Fig. S4. Comparison of capacity above 0.1 V and below 0.1 V at different current densities. a) BHC b) LHC c) KHC.

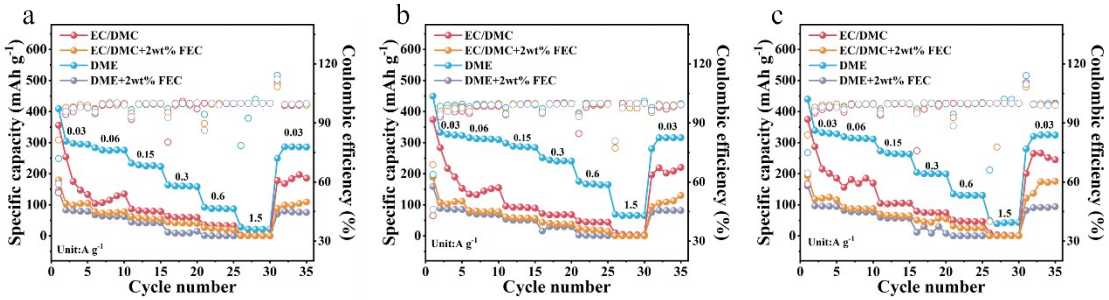

Fig. S5. Rate performance of four electrolytes. a) BHC b) LHC c) KHC.

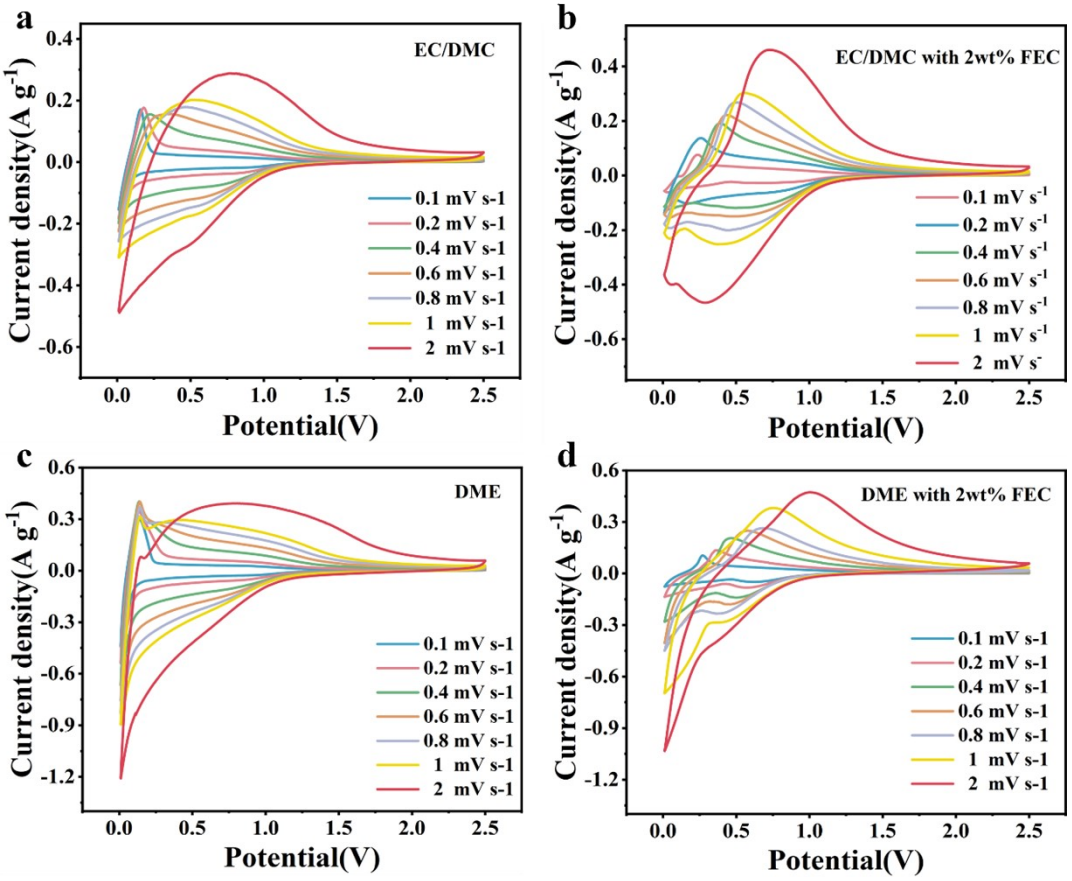

Fig. S6. The CV curves of the SuHC-1200 anode at different scan rates in (a) EC/DMC-based electrolyte. (b) EC/DMC+2wt%FEC-based electrolyte. (c) DME-based electrolyte. (d) DME+2wt%FEC-based electrolyte.

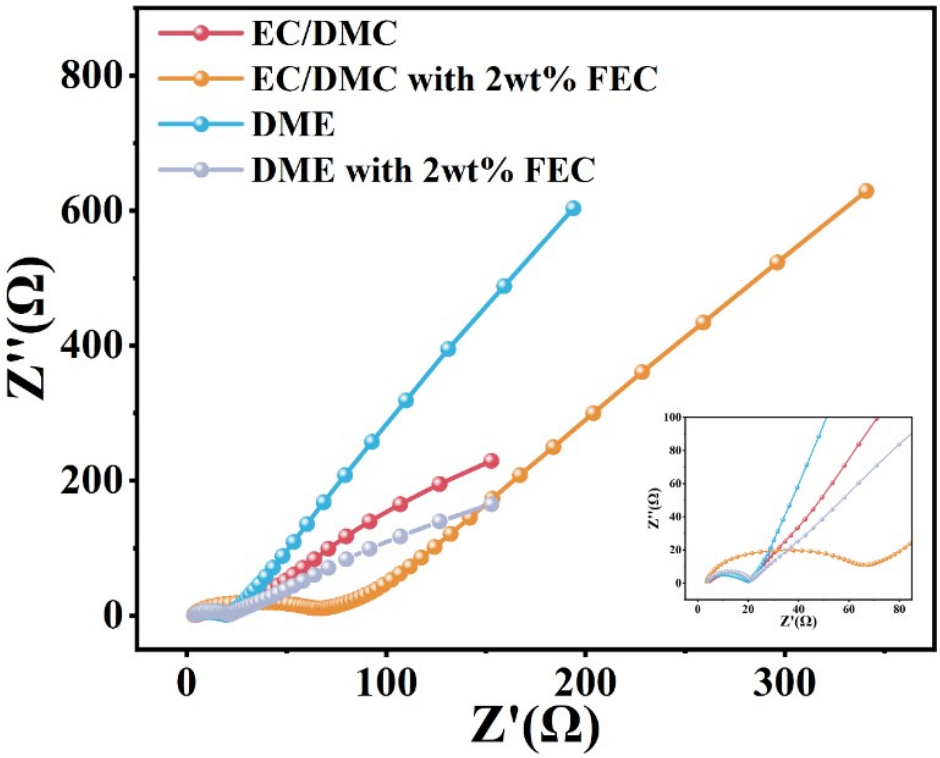

Fig. S7. ElS analysis of discharged SuHC-1200 electrodes in diferent electrolytes.

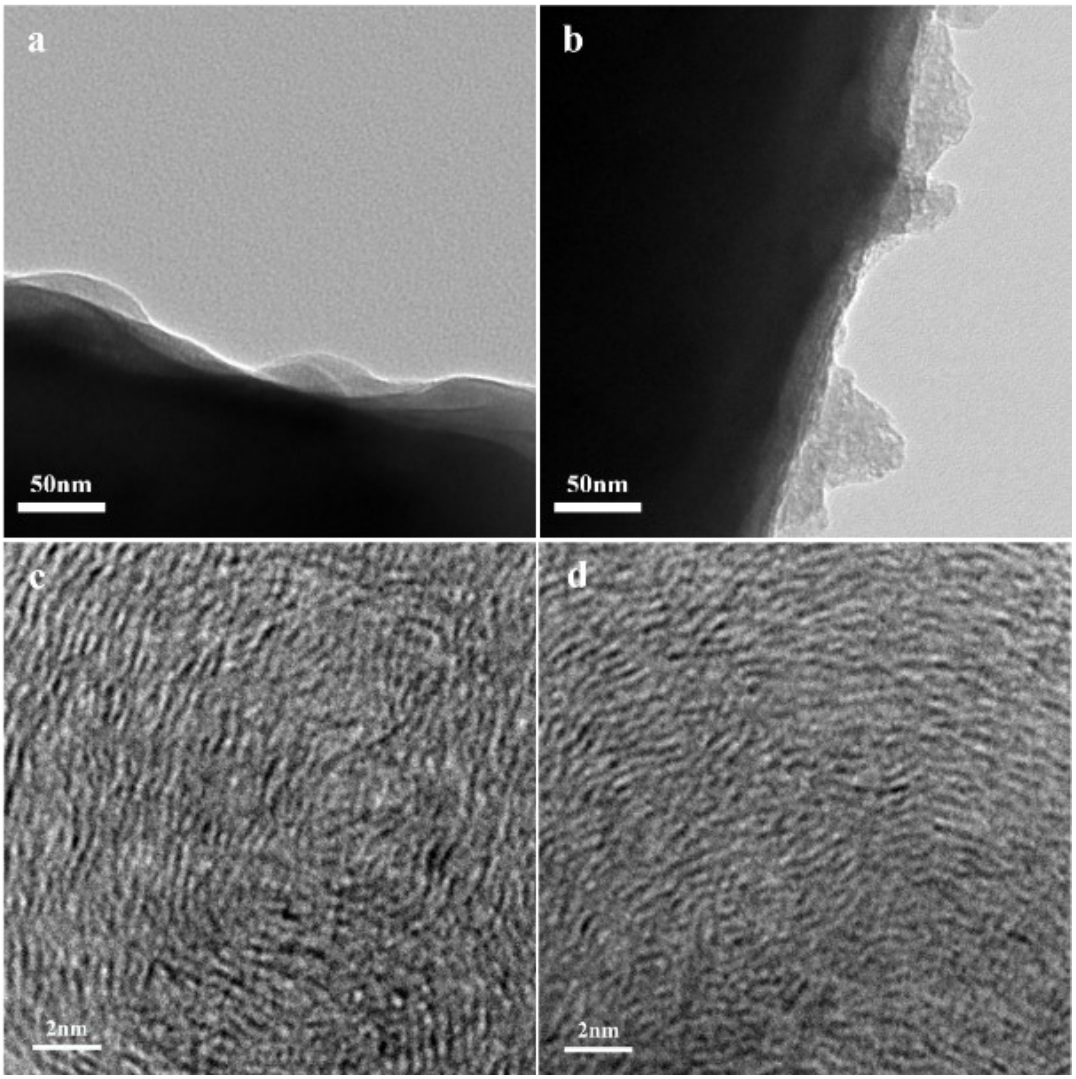

Fig. S8. TEM images in EC/DMC-based electrodes of SuHC-1200 after 3 cycles at 0.03A g^{-1}.

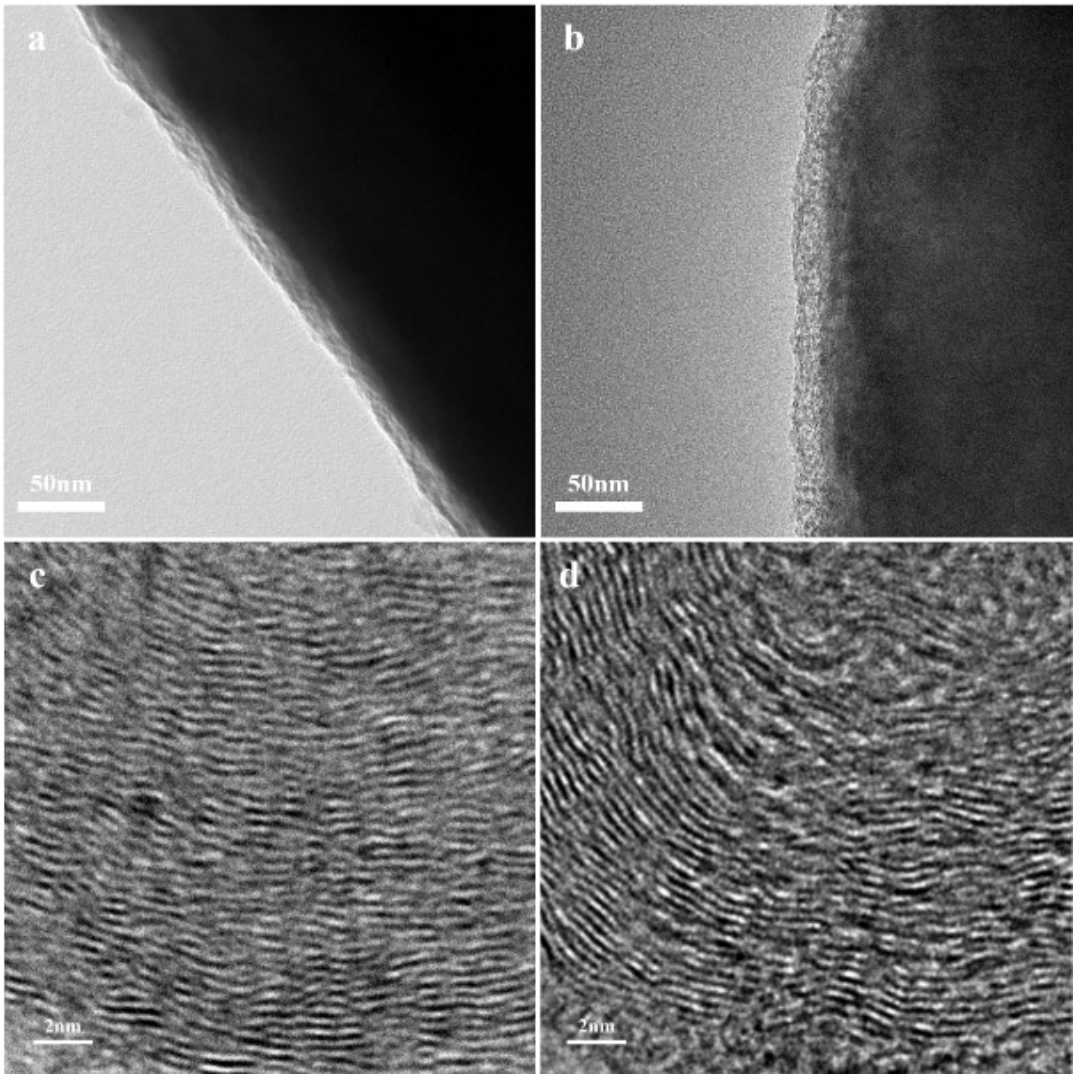

Fig. S9. TEM images in DME-based electrodes of SuHC-1200 after 3 cycles at 0.03A g^{-1}.

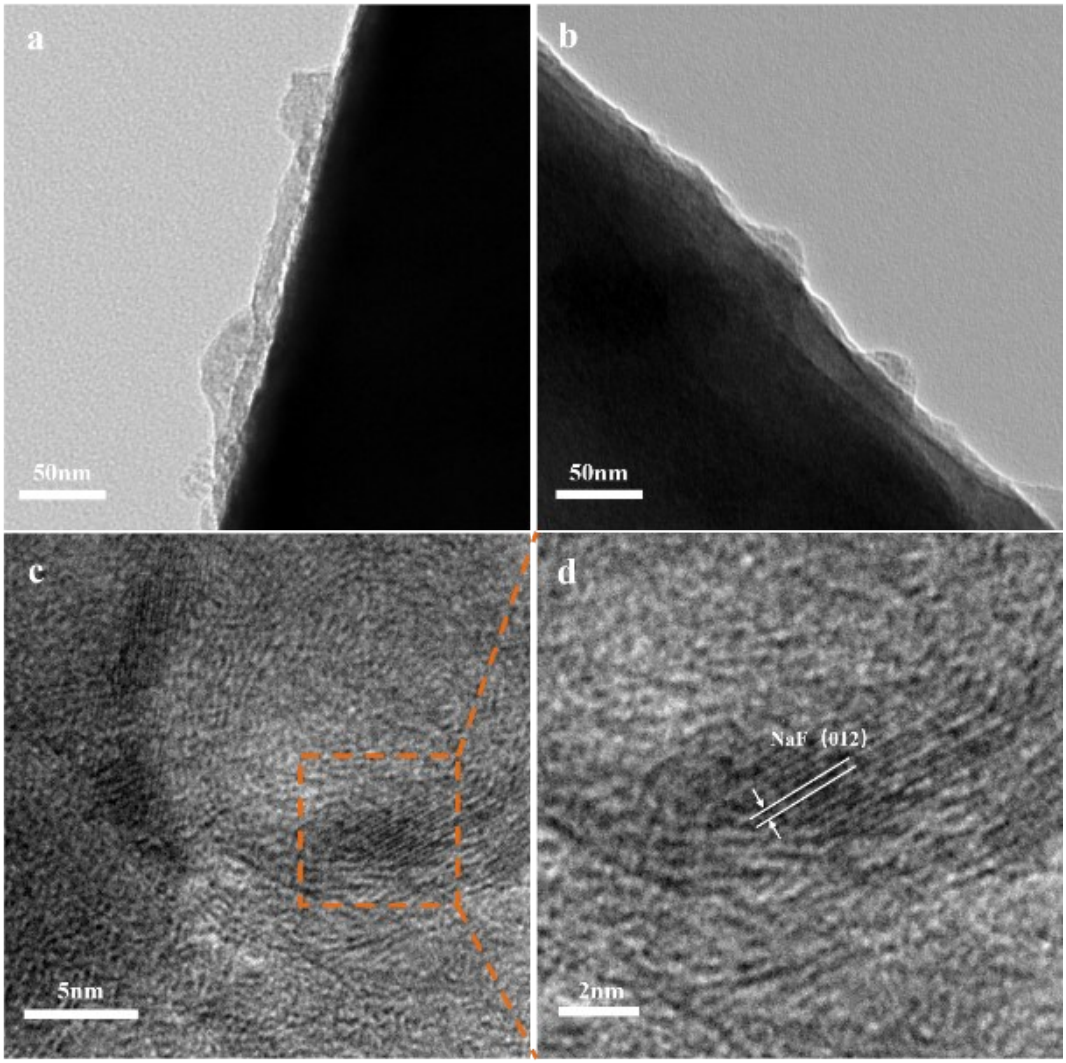

Fig. S10. TEM images in EC/DMC+2wt%FEC-based electrodes of SuHC-1200 after 3 cycles at 0.03A g^{-1}.

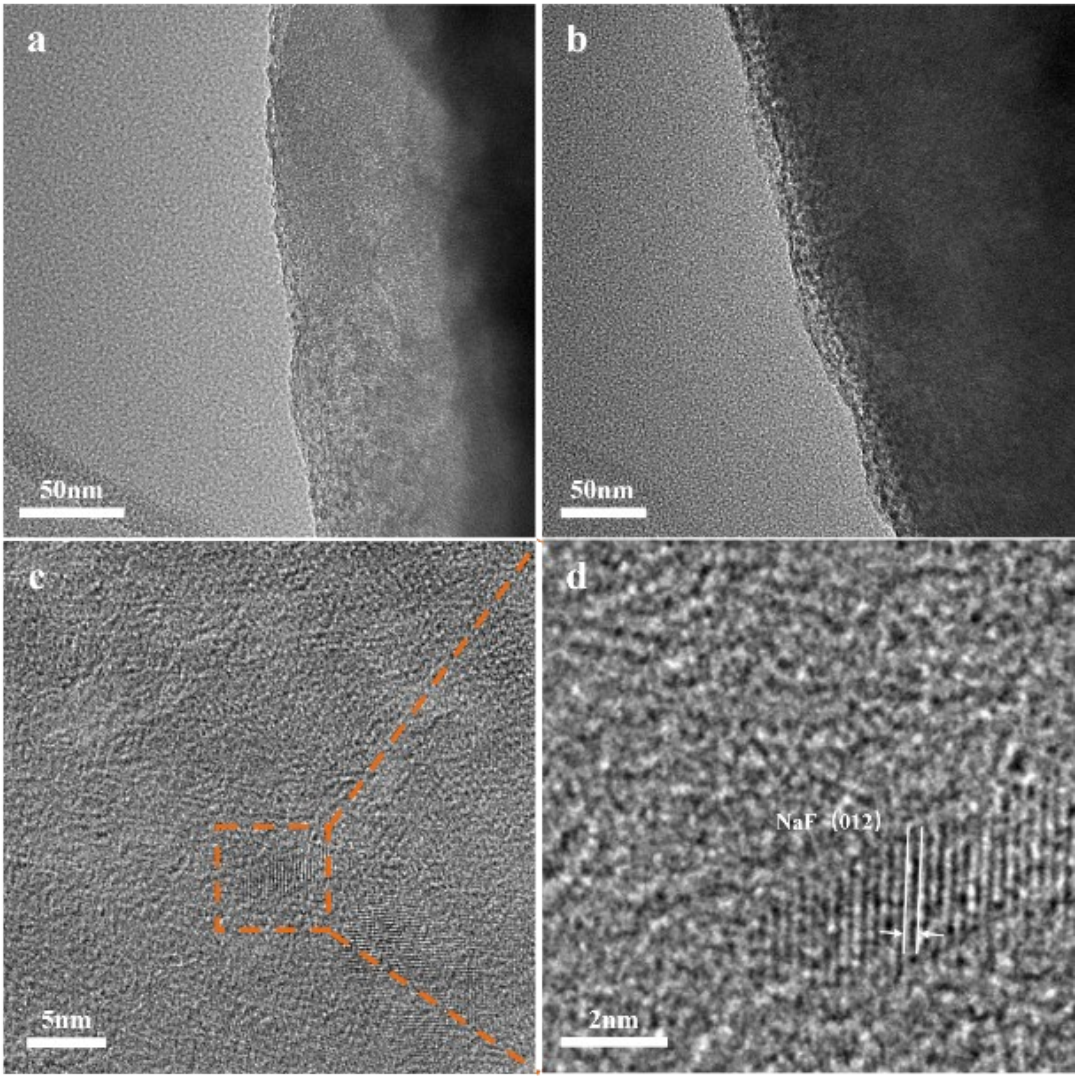

Fig. S11. TEM images in DME+2wt%FEC-based electrodes of SuHC-1200 after 3 cycles at 0.03A g^{-1}.

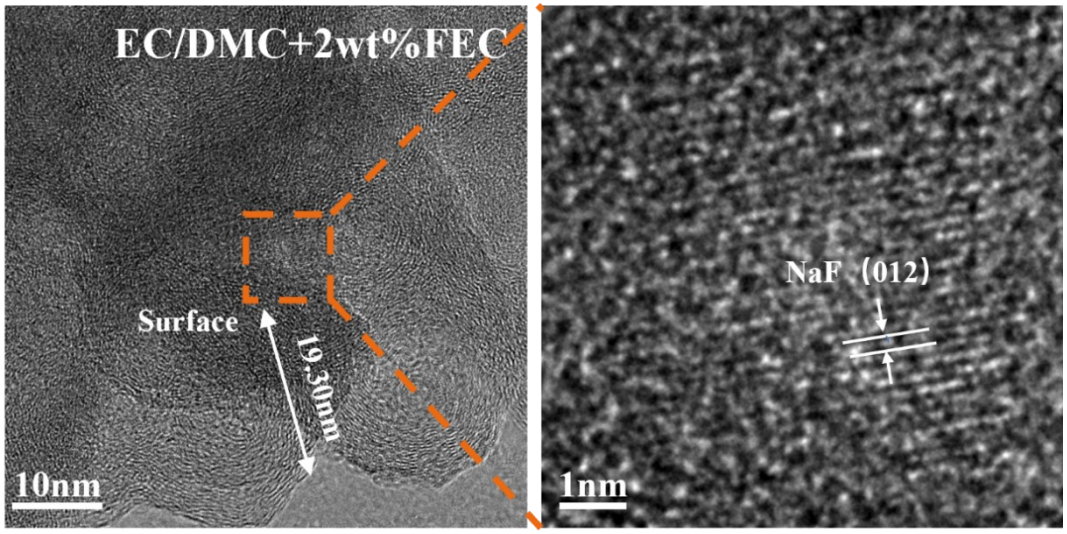

Fig. S12. TEM images in EC/DMC+2wt%FEC-based electrodes of BHC after 3 cycles at 0.03A g^{-1}.

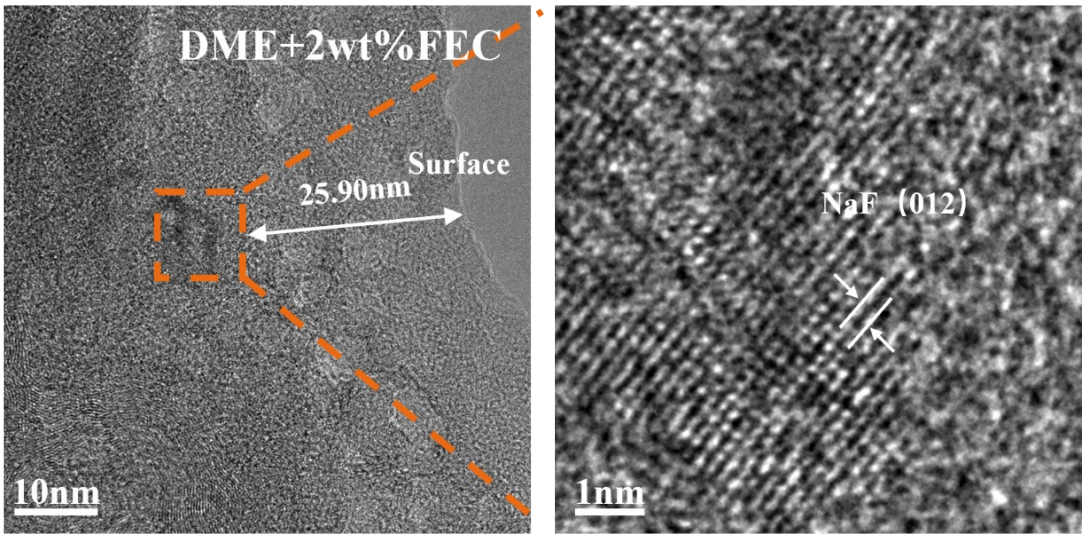

Fig. S13. TEM images in DME+2wt%FEC-based electrodes of BHC after 3 cycles at 0.03A g^{-1}.

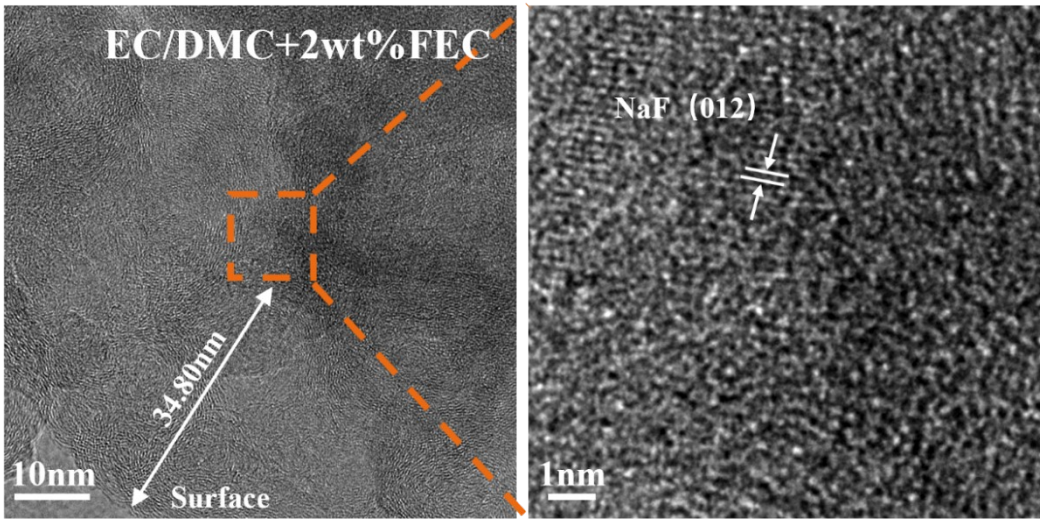

Fig. S14. TEM images in EC/DMC+2wt%FEC-based electrodes of LHC after 3 cycles at 0.03A g^{-1}.

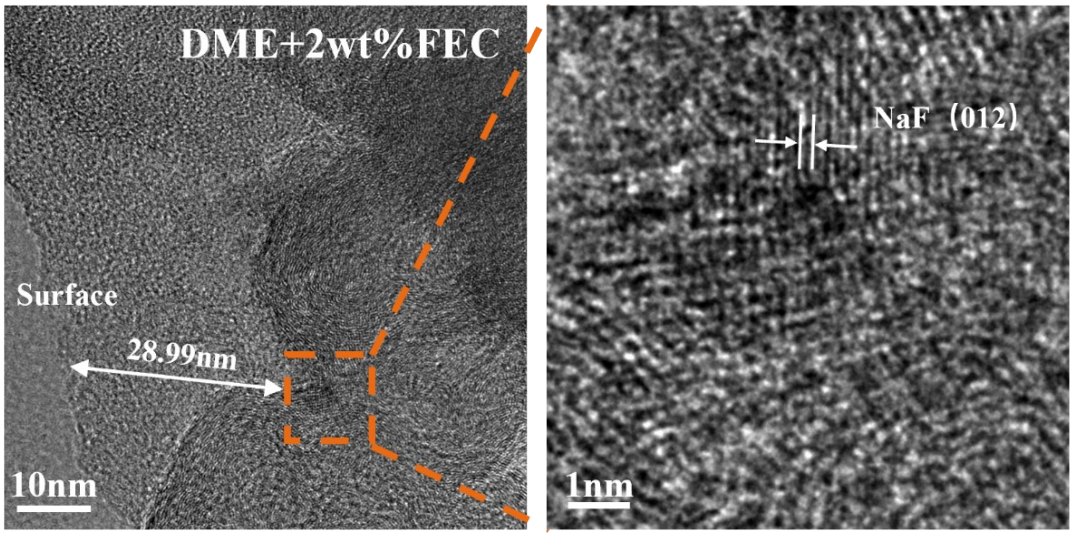

Fig. S15. TEM images in DME+2wt%FEC-based electrodes of LHC after 3 cycles at 0.03A g^{-1}.

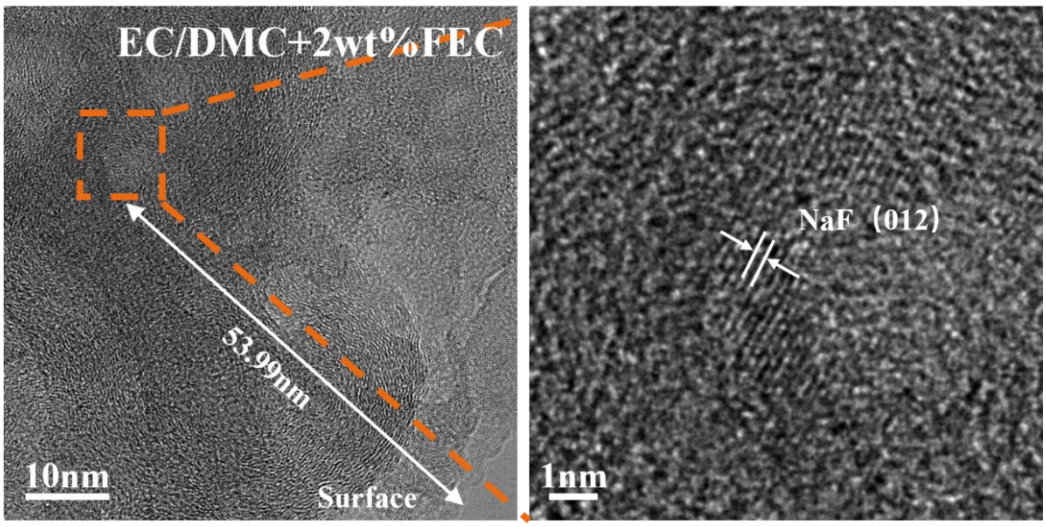

Fig. S16. TEM images in EC/DMC+2wt%FEC-based electrodes of KHC after 3 cycles at 0.03A g^{-1}.

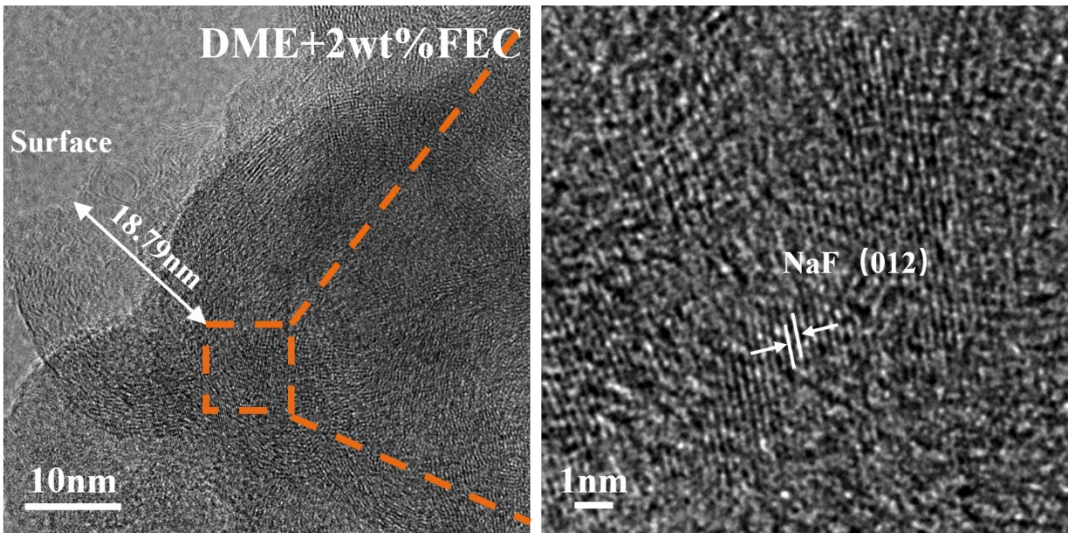

Fig. S17. TEM images in DME+2wt%FEC-based electrodes of KHC after 3 cycles at 0.03A g^{-1}.

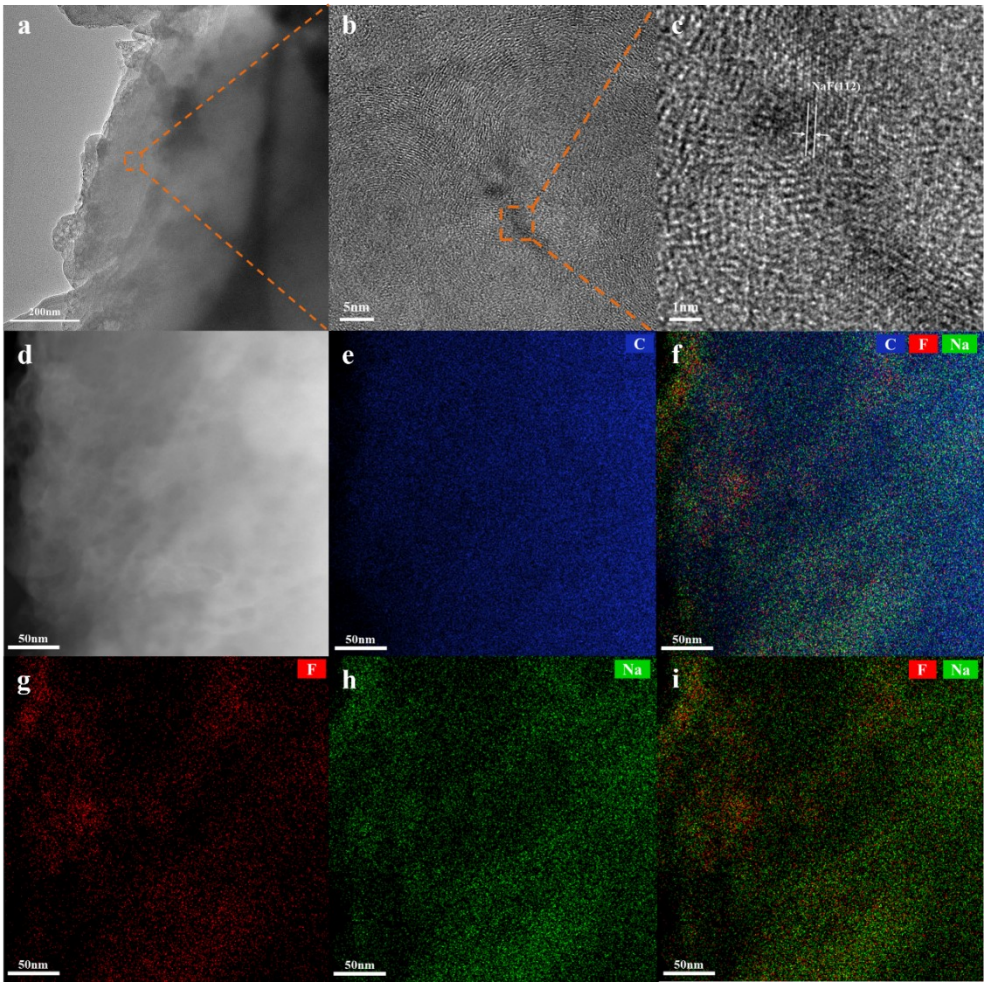

Fig. S18. a-c) TEM images in EC/DMC+2wt%FEC-based electrodes of SuHC-1200 after 3 cycles at 0.03A g^{-1} d-i) Elemental mapping results of SuHC-1200.

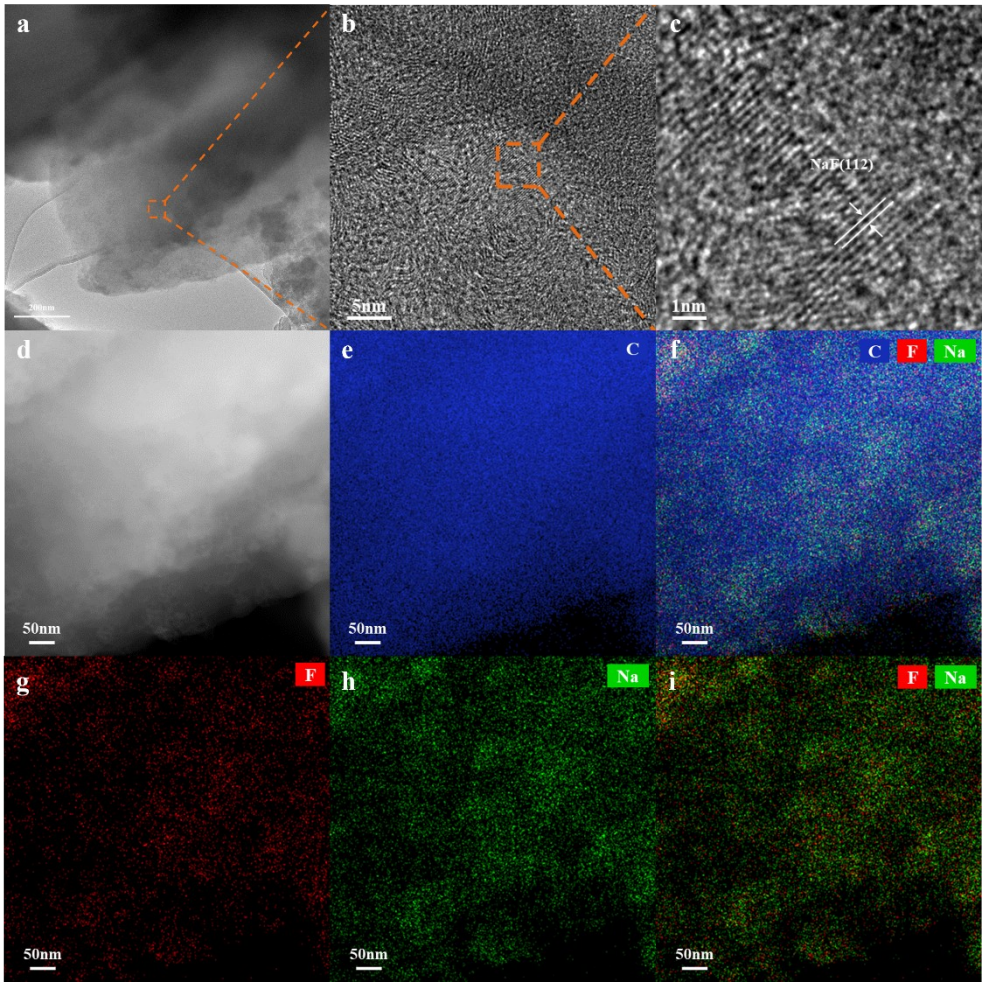

Fig. S19. a-c) TEM images in DME+2wt%FEC-based electrodes of SuHC-1200 after 3 cycles at 0.03A g^{-1} d-i) Elemental mapping results of SuHC-1200.

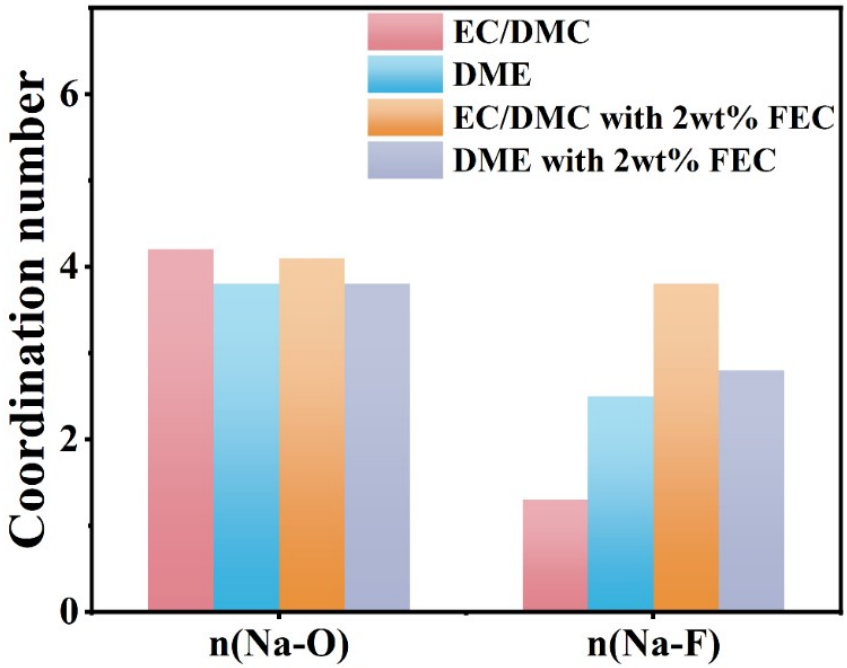

Fig. S20. Average coordination numbers of Na-O and Na-F for EC/DMC、DME、EC/DMC+2wt%FEC and DME+2wt%FEC-based electrolytes.

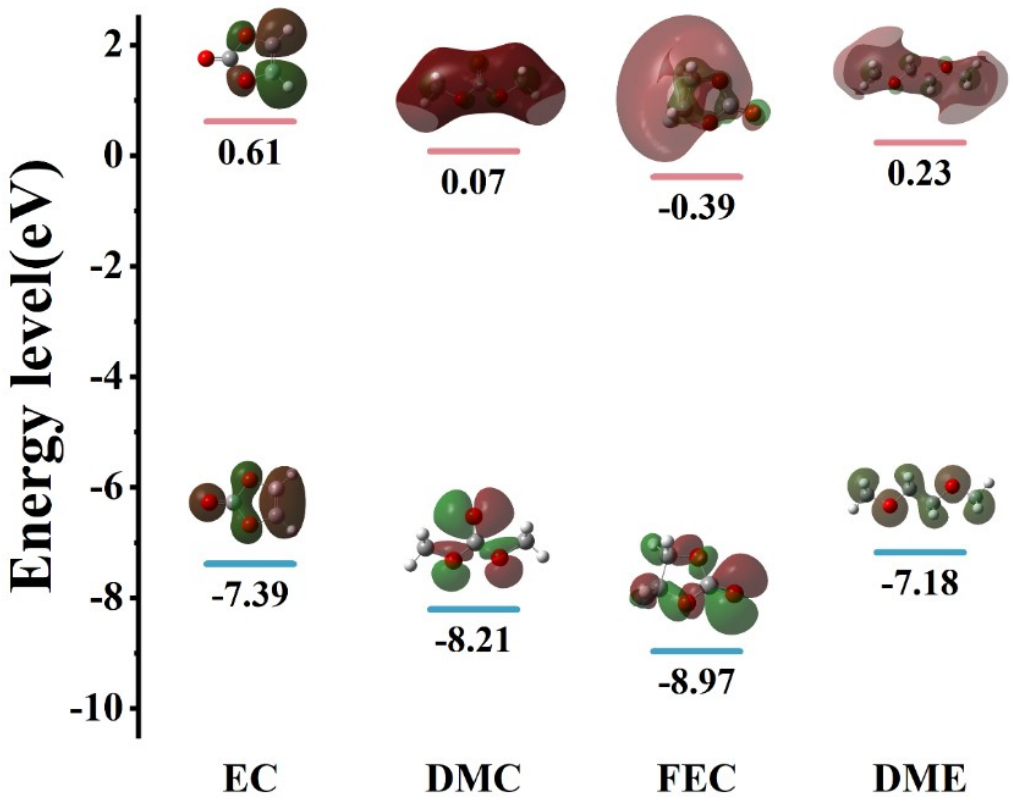

Fig. S21. HOMO and LUMO for electrolytes.

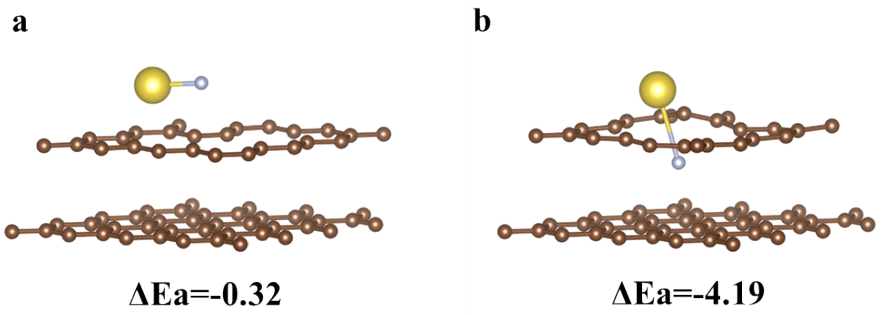

Fig. S22. Side views of the simulation results of NaF molecules on the large pore surface as well as inside the large pore of the carbon material and their corresponding average adsorption energies (ΔEa)

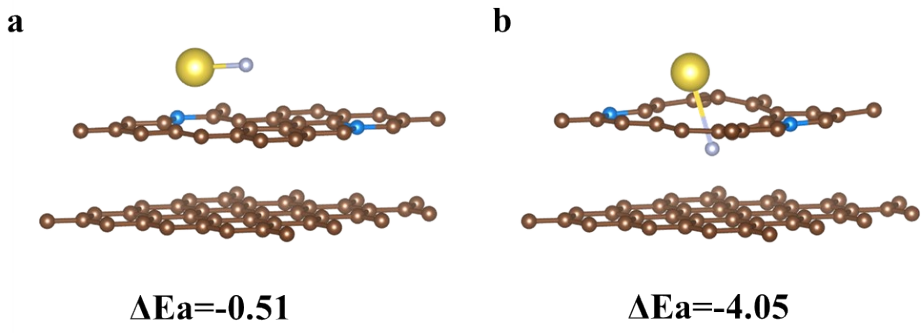

Fig. S23. Side views of the simulation results of NaF molecules on the pore surface as well as inside the pores of the N-doped carbon material and their corresponding average adsorption energies (ΔEa)

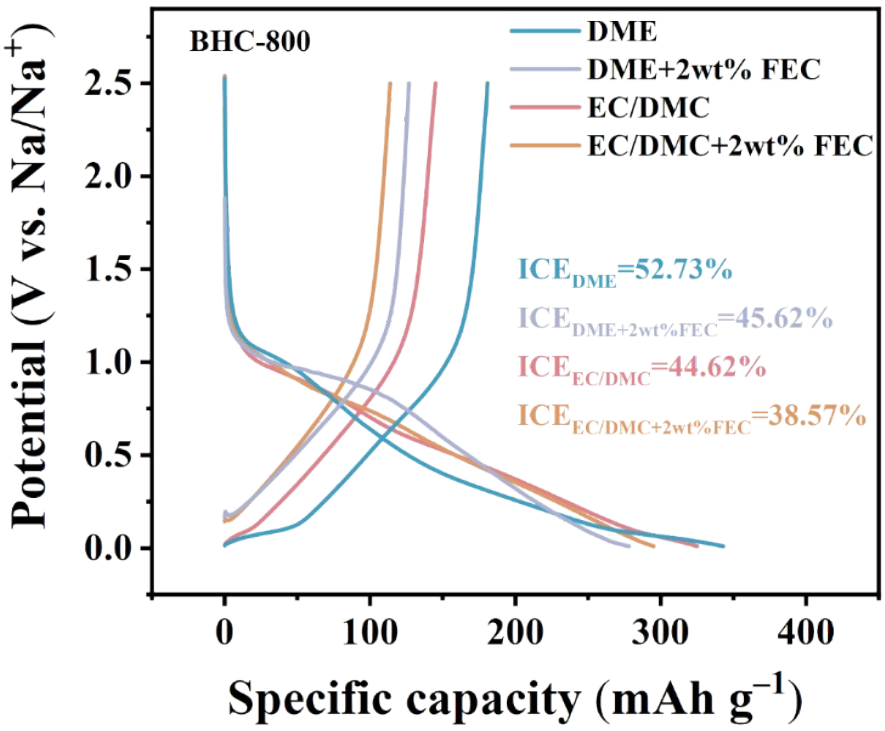

Fig. S24. First charge/discharge curves of SuHC-800 cycled at 30mA g^{-1} in different electrolytes.

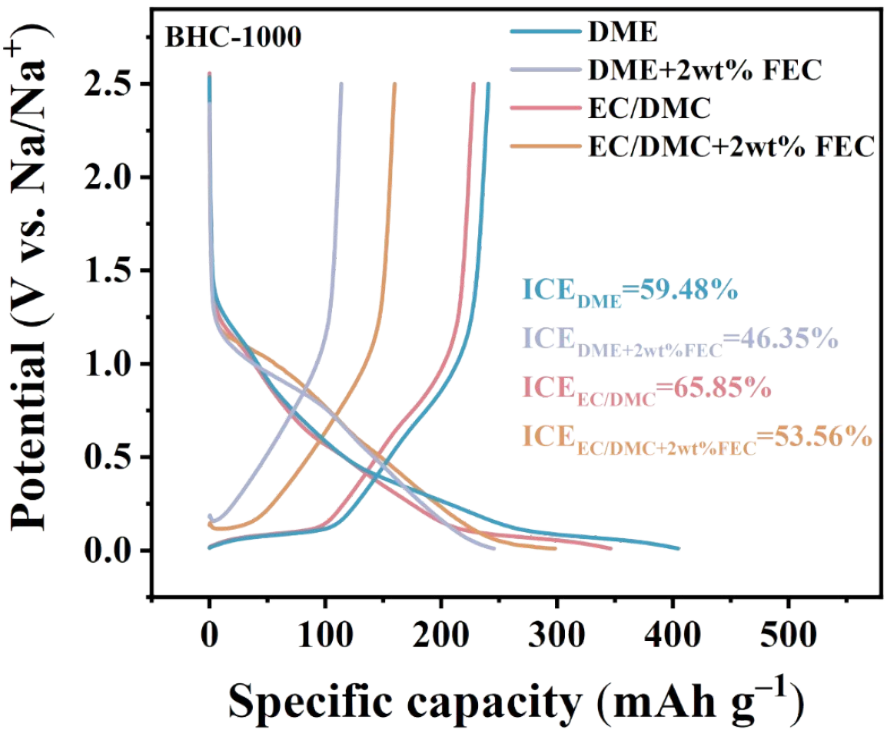

Fig. S25. First charge/discharge curves of SuHC-1000 cycled at 30mA g^{-1} in different electrolytes.

Table S1. Pore structure of the samples.

Samples	SSA($m^2 \cdot g^{-1}$)	Pore volume($cm^3 \cdot g^{-1}$)	Pore width(nm)
BHC-800	33.6	0.049	6.63
BHC-1000	29.6	0.037	4.36
BHC-1200	11.6	0.029	1.87

References

[1] M. Liu, Z. Jiang, X. Wu, F. Liu, W. Li, D. Meng, A. Wei, P. Nie, W. Zhang, W. Zheng, *Angewandte Chemie International Edition* **2025**, *64*, e202425507.

[2] Q. Bai, L. Yang, H. Chen, Y. Mo, *Advanced energy materials* **2018**, *8*, 1702998.

[3] B. Thapa, H. B. Schlegel, *The Journal of Physical Chemistry A* **2016**, *120*, 5726-5735.

[4] Z. Lu, J. Wang, W. Feng, X. Yin, X. Feng, S. Zhao, C. Li, R. Wang, Q. A. Huang, Y. Zhao, *Advanced Materials* **2023**, *35*, 2211461.

[5] X. Lu, J. Zhou, X. Li, H. Peng, C. Shi, F. Liu, L. Huang, Z. Sun, *ACS Applied Materials & Interfaces* **2025**, *17*, 29708-29719.

[6] C. Wang, B. Li, W. Shen, F. Kang, Z. H. Huang, R. Lv, *Advanced Functional Materials* **2023**, *33*, 2214429.